Tuning of the electron g factor in defect-free GaAs nanodisks

Li-Wei Yang,[1] Yi-Chia Tsai,[2] Yiming Li,[2,3] Akio Higo,[3] Akihiro Murayama,[4,5] S. Samukawa,[3,6,*] and O. Voskoboynikov[1,3,†]

[1]*Department of Electronic Engineering and Institute of Electronics, National Chiao Tung University, 1001 Ta Hsueh Road, Hsinchu 300, Taiwan*

[2]*Department of Electrical and Computer Engineering, National Chiao Tung University, 1001 Ta Hsueh Road, Hsinchu 300, Taiwan*

[3]*WPI-Advanced Institute for Materials Research, Tohoku University, Aoba-ku, Sendai, Miyagi 9808577, Japan*

[4]*Graduate School of Information Science and Technology, Hokkaido University, Kita 14, Nishi 9, Kita-ku, Sapporo, Japan*

[5]*CREST Japan Science and Technology Agency, 5 Sanbancho Chiyoda-ku, Tokyo, Japan*

[6]*Institute of Fluid Science, Tohoku University, Aoba-ku, Sendai, Miyagi 9808577, Japan*

(Received 7 October 2015; published 15 December 2015; corrected 29 December 2015)

We theoretically study the impact of changes in surroundings on the electron ground-state effective g factor in defect-free GaAs/AlGaAs nanodisks. To perform the study, we formulate and deploy a computational efficient full three-dimensional model to describe the effective g-factor tensor in semiconductor nano-objects of complex geometry and material content. This model is based on an effective 2×2 conduction-band Hamiltonian which includes the Rashba and Dresselhaus spin-orbit couplings. The description is suited to clarify the important question of the controllability of the electron effective g factor in semiconductor nano-objects. The results of this theoretical study suggest that in the defect-free GaAs/AlGaAs nanodisks, the effective g factor can be tuned within a wide range by proper design of the nanodisk environment. The zz components of the electron effective g-factor tensor obtained in our simulation are in good agreement with some recent experimental observations.

DOI: 10.1103/PhysRevB.92.245423 PACS number(s): 71.70.Ej, 73.22.Dj, 75.70.Tj

I. INTRODUCTION

Semiconductor nano-objects, such as self-assembled quantum dots, quantum rings, quantum-dot molecules, nanowires, etc. (see, for instance, Refs. [1–5], and references therein), offer promising possibilities to control and manipulate electron spins confined in the objects [5–7]. This can be exploited in semiconductor-based quantum information processing and, more widely, in semiconductor-based spintronics [8–16].

Static and dynamic control of isolated electron spins in semiconductor nano-objects can be achieved through coupling of the electron momentum to the particle spins, which is provided by the spin-orbit interaction [17–19]. For instance, the electron spin control (due to the strong spin-orbit interaction) has been demonstrated recently in pure wurtzite InAs nanowire quantum dots [9] and self-assembled InAs quantum dots [20,21].

The Zeeman splitting ΔE for the electron energy states in semiconductor nano-objects at nonzero magnetic field B is characterized by the effective Landé factor (g factor), which can be defined as $g = \Delta E/\mu_B B$ (μ_B is the Bohr magneton). Robust spin manipulations and spin-based qubit operations [8] by an external electric/magnetic field in semiconductor nano-objects require proper techniques to control the particles' effective g factors. Hence, it is crucial to develop a microscopic understanding of the influence of the geometrical and material parameters of the nano-objects on the spin-orbit coupling and magnetic response of individual carriers confined in the objects.

The effective g factor of electrons and holes confined in semiconductor nanostructures (mainly InAs/GaAs and GaAs/AlGaAs quantum wells and quantum dots) was recently extensively studied both theoretically and experimentally (see, for instance, Refs. [20–34] and numerous references therein). It was found that in general in self-assembled semiconductor quantum dots, the effective g factor becomes anisotropic and significantly depends on the direction of the magnetic field in the quantum structures. Hence, it is represented as a tensor with components g_{ij}. The tensor is very sensitive to the geometrical and material parameters of the nanostructures. At the same time, utilization of the electron spins in semiconductor quantum dots requires precise, coherent, and selective control of single electron spin states in arrays of the dots. Therefore, robust engineering and controllability of the g factor of the carriers confined in the quantum dots are fundamental prerequisites in this research domain.

The newly developed biotemplate and neutral-beam etching fusion top-down process can immediately provide us with nanoscale structures of precisely controlled geometrical and material characteristics [35]. Recently, using this process, strain- and defect-free high-quality GaAs/Al_xGa_{1-x}As nanodisks (NDs) have been fabricated with a precise control of the disks' geometrical and material parameters [36–38]. It is known that the effective g factor of electrons in low-dimensional GaAs/Al_xGa_{1-x}As structures (according to a structure's actual geometrical and material parameters) may change from the small negative value $g_{\mathrm{GaAs}} \approx -0.44$ to a positive one of similar absolute value [22,39]. Therefore, the GaAs-based nanosystems could be potentially useful in quantum repeaters for large-scale quantum information networks [33,40]. From this point of view, uniform arrays of the defect-free NDs can be considered as "test-bed" systems in which precise selective and coherent control of the electron (hole) spin states could be ultimately achieved.

Very recently, the electron effective g factor in GaAs NDs fabricated by damage-free neutral-beam etching using bionanotemplates was studied by means of time-resolved Kerr rotation [38] (see Fig. 1). It was suggested that the

*samukawa@ifs.tohoku.ac.jp

†Corresponding author: vam@faculty.nctu.edu.tw

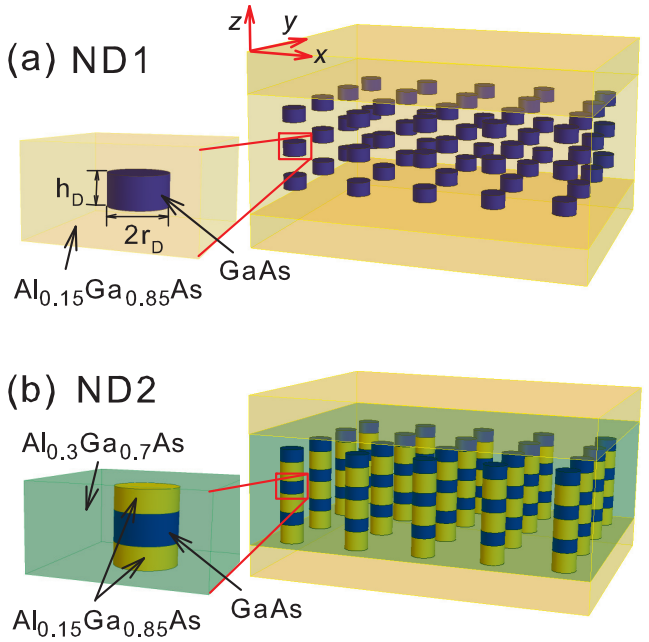

FIG. 1. (Color online) Arrays of the defect-free GaAs NDs as in Ref. [38]. Two types of the arrays are presented: (a) isotropic surroundings of a ND and (b) anisotropic surroundings of a ND.

experimentally obtained magnitude of the electron effective g factor is controlled by the interplay between the vertical (along the system growth direction, i.e., the z direction) and lateral confinement of the electron wave function. In addition, it was assumed that the bulk values of the g factor in the different material domains can be taken for an evaluation of the effective g factor. In this very poor approximation, the electron g factor in semiconductor multidomain nanostructures is estimated as a material average [39],

$$g_{av} = \sum_i g_{el,i}\, p_i, \tag{1}$$

where $g_{el,i}$ is the electron g factor of bulk material in the corresponding domain and

$$p_i = \int_{V_i} d^3\mathbf{r} |\Psi_{el}(\mathbf{r})|^2$$

is the probability to find the electron in the state $\Psi_{el}(\mathbf{r})$ inside the ith domain with the volume V_i. However, this estimate neglects changes in the electron and hole energy states in the confinement regime and cannot explain the anisotropy of the g-factor tensor in nanosystems.

In general, the electron effective g factor can be determined accurately by the second-order $\mathbf{k}\cdot\mathbf{p}$ theory using Roth's formula [41,42]. In bulk zinc-blende III-V semiconductors, only the upper valence bands give the main contribution to the electron effective g factor. Therefore, within the 8×8 $\mathbf{k}\cdot\mathbf{p}$ theory, the effective electron bulk g factor is

$$g_B = g_0 - \frac{2E_P}{3}\frac{\Delta}{E_g(E_g+\Delta)}, \tag{2}$$

where g_0 is the free electron Landé factor, E_P is the Kane interband coupling parameter, E_g is the band gap, and Δ is the spin-orbit coupling energy. This expression nearly reproduces (with a small relative deviation from experimental data) the electron effective g factor for narrow-gap III-V semiconductors (InSb, InAs). However, for semiconductors with relatively wide gaps (e.g., GaAs), Eq. (2) requires considerable corrections (about 27% for bulk GaAs) due to all of the remote bands not included in the $\mathbf{k}\cdot\mathbf{p}$ 8×8 Hamiltonian [39,42–44].

For electrons confined in semiconductor nano-objects, the Roth's equation is a sum over all energy states including heavy, light, and spin-off hole excited states. This procedure barely converges in simulation (or does not converge at all) for most of the semiconductor nanostructures. In addition, commonly used for the direct band-gap zinc-blende heterostructures, the $\mathbf{k}\cdot\mathbf{p}$ 8×8 Hamiltonian models may numerically result in spurious unphysical solutions. The models require renormalizations and corrections of the material constants for each specific case (see, for instance, Refs. [19,45–47], and references therein). This is really troublesome for the physical analysis in the case of GaAs nano-objects of multidomain complex geometry and material content, when the actual value of the electron effective g factor is varying within a neighborhood of zero. Nevertheless, appropriate and successful simulation has been performed for the electron g factor in strain-free semiconductor GaAs/Al_xGa_{1-x}As quantum wells and quantum dots of relatively simple geometry and material content. In the simulation, the Kane 8×8 Hamiltonian and 2×2 conduction-band model were used (see, for instance, Refs. [22,39,48–50]). Unfortunately, the former approach cannot guarantee nonspurious solutions for the desirable range of material parameters and the latter one requires material parameters that could hardly be verified from the literature.

In this paper, we develop an efficient approach to model and analyze the effective g factor for electrons confined in zinc-blende semiconductor complex multidomain nanostructures (such as defect-free GaAs nanodisks of different configurations). In the approach, we employ an effective 2×2 conduction-band Hamiltonian including the Rashba and Dresselhaus spin-orbit interactions. We demonstrate the approach efficiency for simulation and analysis of the electron g-factor tensor in GaAs/Al_xGa_{1-x}As NDs. This makes it possible to theoretically investigate the important issue of the geometrical and material tuning of the effective g factor in the defect-free NDs. The results of this study clearly show that the proposed description and simulation data are appropriate for experiments with uniform arrays of GaAs/Al_xGa_{1-x}As NDs.

II. THEORETICAL MODEL

We describe single electron energy states in III-V semiconductor NDs embedded into a III-V semiconductor matrix in the presence of the external magnetic $\mathbf{B}$ field using the following effective 2×2 conduction-band Hamiltonian which includes the Rashba and Dresselhaus spin-orbit couplings [17–19,51–57]:

$$\hat{\mathbf{H}} = \hat{\mathbf{H}}_e + \hat{\mathbf{H}}_{\text{spin}}. \tag{3}$$

In this Hamiltonian, the spin-independent part is written as

$$\hat{\mathbf{H}}_e = \left[\hat{\mathbf{\Pi}}\frac{1}{2m(\mathbf{r},E)}\hat{\mathbf{\Pi}} + V(\mathbf{r})\right]\hat{\mathbf{I}}_2, \tag{4}$$

and

$$\hat{\mathbf{H}}_{\text{spin}} = \hat{\mathbf{H}}_M + \hat{\mathbf{H}}_R + \hat{\mathbf{H}}_D \tag{5}$$

is the Hamiltonian which is relevant to the electron's spin. In Eq. (5),

$$\hat{\mathbf{H}}_M = \tfrac{1}{2}\mu_B g_B(\mathbf{r},E)\hat{\sigma}\cdot\mathbf{B} \tag{6}$$

is the material Zeeman term,

$$\hat{\mathbf{H}}_R = \nabla_{\mathbf{r}}\beta(\mathbf{r},E)\cdot[\hat{\sigma}\times\hat{\mathbf{\Pi}}] \tag{7}$$

presents the Rashba spin-orbit interaction, and

$$\hat{\mathbf{H}}_D = \frac{b_{41}^{6c6c}(\mathbf{r})}{\hbar^3}\left[\hat{\sigma}_x\hat{\Pi}_x\left(\hat{\Pi}_y^2-\hat{\Pi}_z^2\right)+\hat{\sigma}_y\hat{\Pi}_y\left(\hat{\Pi}_z^2-\hat{\Pi}_x^2\right)+\hat{\sigma}_z\hat{\Pi}_z\left(\hat{\Pi}_x^2-\hat{\Pi}_y^2\right)\right] \tag{8}$$

stands for the Dresselhaus spin-orbit interaction. In the equations above, $\hat{\mathbf{I}}_2$ is the identity matrix of size 2, $\mathbf{r}=(x,y,z)$ is the three-dimensional radius vector,

$$\hat{\Pi} = -i\hbar\nabla_{\mathbf{r}} + e\mathbf{A}(\mathbf{r}) \tag{9}$$

stands for the momentum operator of electrons, $\nabla_{\mathbf{r}} = (\nabla_x,\nabla_y,\nabla_z)$ is the spatial gradient, $\mathbf{A}(\mathbf{r})$ is the vector potential of the magnetic field $\mathbf{B}=\nabla_{\mathbf{r}}\times\mathbf{A}(\mathbf{r})$,

$$V(\mathbf{r}) = \begin{cases} 0 & \text{inside ND} \\ \Delta E_c(\mathbf{r}) & \text{outside ND} \end{cases} \tag{10}$$

is the electron confinement potential [$\Delta E_c(\mathbf{r})$ represents the local conduction-band offset in the structure; see Fig. 2],

$$\frac{1}{m(\mathbf{r},E)} = \frac{1}{3m_0}\frac{E_P(\mathbf{r})[3\tilde{E}_g(\mathbf{r},E)+2\Delta(\mathbf{r})]}{\tilde{E}_g(\mathbf{r},E)[\tilde{E}_g(\mathbf{r},E)+\Delta(\mathbf{r})]} \tag{11}$$

and

$$g_B(\mathbf{r},E) = g_0 - \frac{2}{3}\frac{E_P(\mathbf{r})\Delta(\mathbf{r})}{\tilde{E}_g(\mathbf{r},E)[\tilde{E}_g(\mathbf{r},E)+\Delta(\mathbf{r})]} \tag{12}$$

are the electron energy- and position-dependent effective mass and bulk Landé factor,

$$\beta(\mathbf{r},E) = \frac{\hbar}{4m_0}[g_0 - g_B(\mathbf{r},E)] \tag{13}$$

is the Rasba spin-orbit coupling parameter [19,52,53,56], and

$$\tilde{E}_g(\mathbf{r},E) = \begin{cases} E+E_g^{\text{in}} & \text{inside ND} \\ E+E_g^{\text{in}}+\Delta E_v(\mathbf{r}) & \text{outside ND} \end{cases} \tag{14}$$

is the effective band gap in the structure [$\Delta E_v(\mathbf{r})$ stands for the local valence-band offset; see Fig. 2]. The position-dependent spin-orbit splitting for the valence bands is taken to be $\Delta(\mathbf{r})$, $E_p(\mathbf{r})$ is the position-dependent Kane interband coupling parameter, $b_{41}^{6c6c}(\mathbf{r})$ is the Dresselhaus coefficient [19], $\hat{\sigma}$ is the vector of the Pauli matrices, and m_0 and e are the free electron mass and elementary charge, respectively. In this paper, we consider symmetrical and asymmetrical environment for the NDs (see below). Therefore, we adopt a gauge-origin-independent definition for the vector potential (see Ref. [58], and references therein): $\mathbf{A}(\mathbf{r}) = \mathbf{B}\times(\mathbf{r}-\bar{\mathbf{r}})/2$, where $\bar{\mathbf{r}}$ stands

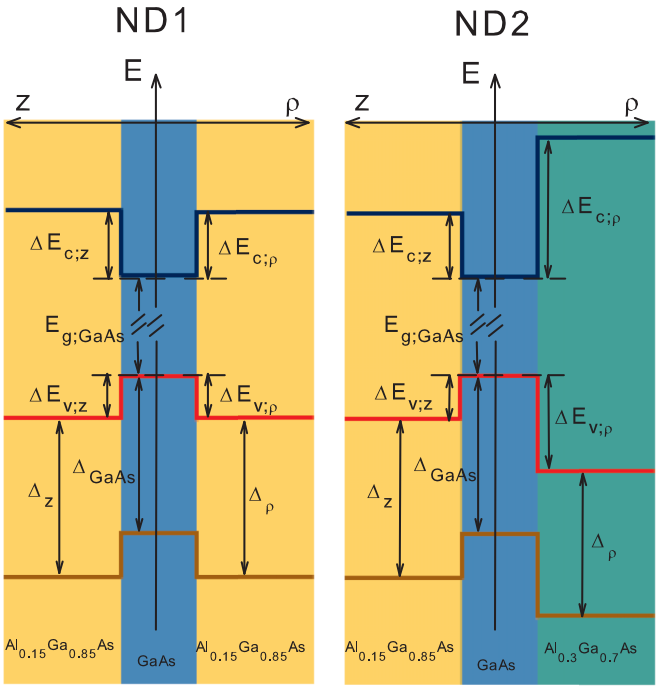

FIG. 2. (Color online) Schematic of the conduction- and valence-band profiles in the structures involving ND1 and ND2 ($\rho=\sqrt{x^2+y^2}$).

for the expectation value of the position of the electron in the ground state. Using this gauge and Eqs. (5)–(8) for a weak external magnetic field ($B\to 0$), the spin-dependent part of the electron Hamiltonian (after some algebra for the linear approximation, keeping only the first order of the magnetic field B, and including corrections due to all of the remote bands) can be written in the following form [39]:

$$\hat{\mathbf{H}}_{\text{spin}} \approx \hat{\mathbf{H}}_{\text{spin}}^{B=0} + \frac{1}{2}\mu_B\sum_{i,j=x,y,z}\hat{g}_{ij}(\mathbf{r},E)\hat{\sigma}_i B_j, \tag{15}$$

where

$$\hat{\mathbf{H}}_{\text{spin}}^{B=0} = -i\hbar\nabla_{\mathbf{r}}\beta(\mathbf{r},E)\cdot[\hat{\sigma}\times\nabla_{\mathbf{r}}] + b_{41}^{6c6c}(\mathbf{r})\left[\hat{\sigma}_x\nabla_x\left(\nabla_y^2-\nabla_z^2\right)+\hat{\sigma}_y\nabla_y\left(\nabla_z^2-\nabla_x^2\right)+\hat{\sigma}_z\nabla_z\left(\nabla_x^2-\nabla_y^2\right)\right], \tag{16}$$

and the components of the effective g-factor tensor are defined as

$$\hat{g}_{ij}(\mathbf{r},E) = [g_B(\mathbf{r},E)+\delta g_B(\mathbf{r})]\delta_{ij} + g_{ij}^R(\mathbf{r},E) + g_{ij}^D(\mathbf{r},E). \tag{17}$$

In Eq. (17), $\delta g_B(\mathbf{r})$ stands for the position-dependent correction due to all of the remote bands. The Rashba and Dresselhaus couplings bring correspondingly the components g_{ij}^R and g_{ij}^D to the g tensor:

$$\hat{g}^R(\mathbf{r},E) = \begin{pmatrix} \Lambda_{yy}+\Lambda_{zz} & -\Lambda_{yx} & -\Lambda_{zx} \\ -\Lambda_{xy} & \Lambda_{xx}+\Lambda_{zz} & -\Lambda_{zy} \\ -\Lambda_{xz} & -\Lambda_{yz} & \Lambda_{xx}+\Lambda_{yy} \end{pmatrix}, \tag{18}$$

$$\hat{g}^D_{xx}(\mathbf{r}) = 2\gamma(\mathbf{r})(R_z\nabla_x\nabla_y + R_y\nabla_x\nabla_z),$$
$$\hat{g}^D_{xy}(\mathbf{r}) = \gamma(\mathbf{r})\big(-R_z\nabla_y^2 - 2\nabla_z - 2R_x\nabla_x\nabla_z + 2R_z\nabla_z^2\big),$$
$$\hat{g}^D_{xz}(\mathbf{r}) = \gamma(\mathbf{r})\big(-R_y\nabla_z^2 - 2\nabla_y - 2R_x\nabla_x\nabla_y + R_y\nabla_y^2\big),$$
$$\hat{g}^D_{yx}(\mathbf{r}) = \gamma(\mathbf{r})\big(-R_z\nabla_x^2 - 2\nabla_z - 2R_y\nabla_y\nabla_z + R_z\nabla_z^2\big),$$
$$\hat{g}^D_{yy}(\mathbf{r}) = 2\gamma(\mathbf{r})(R_x\nabla_y\nabla_z + R_z\nabla_y\nabla_x),$$
$$\hat{g}^D_{yz}(\mathbf{r}) = \gamma(\mathbf{r})\big(-R_x\nabla_z^2 - 2\nabla_x - 2R_y\nabla_y\nabla_x + R_x\nabla_x^2\big),$$
$$\hat{g}^D_{zx}(\mathbf{r}) = \gamma(\mathbf{r})\big(-R_y\nabla_x^2 - 2\nabla_y - 2R_z\nabla_z\nabla_y + R_y\nabla_y^2\big),$$
$$\hat{g}^D_{zy}(\mathbf{r}) = \gamma(\mathbf{r})\big(-R_x\nabla_y^2 - 2\nabla_x - 2R_z\nabla_z\nabla_x + R_x\nabla_x^2\big),$$
$$\hat{g}^D_{zz}(\mathbf{r}) = 2\gamma(\mathbf{r})(R_y\nabla_z\nabla_x + R_x\nabla_z\nabla_y), \tag{19}$$

where

$$\Lambda_{ij}(\mathbf{r},E) = \tfrac{1}{2}\nabla_i g_B(\mathbf{r},E)\cdot R_j, \tag{20}$$

$R_j = (\mathbf{r}-\bar{\mathbf{r}})_j$, and $\gamma(\mathbf{r}) = m_0\hbar^{-2}b_{41}^{6c6c}(\mathbf{r})$.

For the effective 2×2 Hamiltonian (3), an electron energy state is presented by the two-component spinor,

$$\Phi^{\{2\}}_{n,s}(\mathbf{r}) = \begin{pmatrix} F_{n,s,\uparrow} \\ F_{n,s,\downarrow}\end{pmatrix},$$

where n stands for the main quantum number and s refers to the spin polarization. The envelope wave functions $F_{n,s,\uparrow\downarrow}$ are satisfying the following Schrödinger equation:

$$\hat{\mathbf{H}}\begin{pmatrix} F_{n,s,\uparrow} \\ F_{n,s,\downarrow}\end{pmatrix} = E_{n,s}\begin{pmatrix} F_{n,s,\uparrow} \\ F_{n,s,\downarrow}\end{pmatrix}. \tag{21}$$

Now one can solve the system of nonlinear equations (21) numerically and obtain the dependence of the electron energy (including excited states) on the magnetic field [32,48]. Alternatively, in this paper, to analyze the electron effective g-factor properties at the weak magnetic field, we deploy the advantage of the simulation of the expectation values of the g-tensor components when $B\to 0$ [58–60]. Therefore, to simulate and analyze the g-factor tensor for the ground state of the electron confined in the NDs, we first solve the nonlinear Schrödinger equation with the Hamiltonian presented by Eq. (3) without spin and magnetic field,

$$\left[-\nabla_{\mathbf{r}}\frac{\hbar^2}{2m(\mathbf{r},E_0)}\nabla_{\mathbf{r}} + V(\mathbf{r})\right]\Psi_{E_0}(\mathbf{r}) = E_0\Psi_{E_0}(\mathbf{r}), \tag{22}$$

and obtain the ground-state wave function $\Psi_{E_0}(\mathbf{r})$ and ground-state energy E_0 of the electron confined in NDs. We use this solution to calculate the principal energy-dependent parameter of the system, $\tilde{E}_g(\mathbf{r},E_0)$. Thus, we are able to retrace all information relevant to $\hat{g}(\mathbf{r},E)$. The expectation value of a quantity $\hat{f}(\mathbf{r})$ in the electron ground state with the wave function $\Psi_{E_0}(\mathbf{r})$ is conventionally defined as

$$\bar{f} \equiv \langle f\rangle = \int \Psi^*_{E_0}(\mathbf{r})\hat{f}(\mathbf{r})\,\Psi_{E_0}(\mathbf{r})d\mathbf{r}. \tag{23}$$

Therefore, for a weak magnetic field within the linear approximation, we can simulate and analyze the expectation values of all components of the electron ground-state effective g-factor tensor $g_{ij} = \langle\hat{g}_{ij}(\mathbf{r},E_0)\rangle$ [59,60] and the tensor anisotropy ratio $P_{ij} = (g_{ii}-g_{jj})/(g_{ii}+g_{jj})$.

III. SIMULATION RESULTS AND DISCUSSION

First we simulate the electron ground-state wave function and energy for two types of GaAs/Al_xGa_{1-x}As nanodisks: ND1 and ND2 (see Fig. 1). The electron effective g factor in arrays of these disks were investigated experimentally in Ref. [38] for the magnetic field parallel to the system growth direction, which is chosen to be the z direction in our simulation. Both NDs are suggested to be perfect cylinders with the base radius $r_D = 7.5$ nm and height $h_D = 8$ nm [38]. We put the origin of the coordinate system in the center of the cylinder.

The lateral distance between NDs in the arrays can vary from 20 to 30 nm and the distance between layers is 12 nm [38]. Therefore, in our simulation, we consider the NDs as individually isolated GaAs nano-objects. The main difference in these two kinds of NDs is the disks' material surroundings: isotropic for the ND1 and anisotropic (different in the z and radial directions) for the ND2 (see Figs. 1 and 2).

The principal material parameters for GaAs/AlGaAs heterostructures, which we use in our simulation, are presented in Table I. In addition, we take 60% of the heterostructure local gap difference to be the local conductance-band offset and 40% to be the local valence-band offset in the NDs (Fig. 2).

The energy and wave functions of the electrons confined in the NDs are obtained numerically from a self-consistent solution of Eq. (22) by the iterative method [62,63] using the COMSOL multiphysics package [64]. We use the simulated wave functions and energies to calculate the expectation values of all components of the g-factor tensor for the ground state of the electron confined in the NDs.

Figure 3 shows the three-dimensional distribution of the probability density for the ground state and the ground-state energy of the electron confined in the NDs at zero magnetic field. As the ND environment is changing from the structure of the ND1 to the structure of the ND2 (see Fig. 1), the distribution is transforming from a nearly spherical one (slightly deformed at the edges of the disk) to a considerably squeezed one in the radial direction. This is followed by a substantial increase of the confinement energy (and the effective band gap in the ND).

TABLE I. Material parameters.[a]

Parameter	GaAs	AlAs	$Al_{0.15}Ga_{0.85}As$	$Al_{0.3}Ga_{0.7}As$
E_g (eV)	1.519	3.099	1.686	1.873
E_P (eV)	28.80	21.10	27.65	26.49
Δ (eV)	0.341	0.280	0.332	0.323
ΔE_c (eV)			0.100	0.213
ΔE_v (eV)			0.067	0.142
b_{14}^{6c6c} (eV Å^3)	27.58	18.53	26.22	24.87
g_{el}[b]	−0.445	2.0	0.057	0.475
δ_B[c]	−0.128		−0.144	−0.140

[a]The parameters are taken from [19,25,44,61]. The energy gap E_g of bulk $Al_xGa_{1-x}As$ is interpolated as [25] $E_g = 1.519 + 1.04x + 0.47x^2$. The parameters E_P, Δ, and b_{41}^{6c6c} of bulk $Al_xGa_{1-x}As$ are linearly interpolated as $D_x = xD_{AlAs} + (1-x)D_{GaAs}$.

[b]The electron effective g factor of bulk $Al_xGa_{1-x}As$ is interpolated as [25] $g_{el} \approx -0.445 + 3.38(Eg - 1.519) - 2.21(Eg - 1.519)^2$.

[c]This corrects g_B from Eq. (2) to the actual value g_{el}.

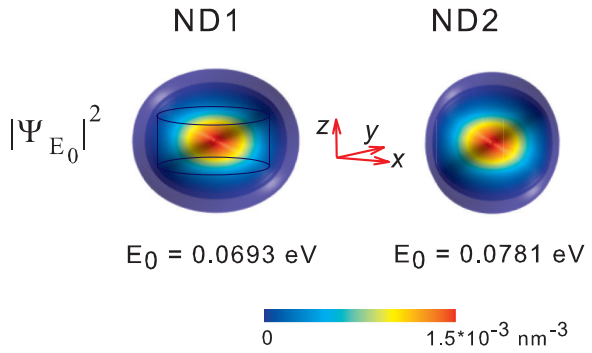

FIG. 3. (Color online) Probability density distribution for the electron ground states in the ND1 and ND2. The electron ground-state energies are presented correspondingly.

For a better understanding of the impact of the environmental changes on the electron wave-function confinement in different directions and overall confinement, we consider the expectation value of the electron characteristic extension (mean) length in the z direction, $d_z = \langle (z-\bar{z})^2\rangle^{1/2}$, expectation value of the mean lateral electron radius, $d_\rho = \langle (x-\bar{x})^2 + (y-\bar{y})^2\rangle^{1/2}$, and overall characteristic length of the electron in the structure, $d = (d_z^2 + d_\rho^2)^{1/2}$. We note that according to the cylindrical and reflection (in the x-z and y-z planes) symmetry of the ND1 and ND2, the expectation value of the position of the electron in the ground state is $\bar{\mathbf{r}} = (0,0,0)$. The computed values of the characteristic lengths are listed in Table II. The changes in the ND's surroundings cause transformations of the electron wave-function extension both in the z and lateral directions, which leads to the overall squeeze of the wave function in the ND2. This is a clear demonstration of the nonseparable ("nonadiabatic") fully three-dimensional behavior of the electron wave function in small nano-objects [65]. The overall squeeze of the wave function is a contradiction to the assumptions made in Ref. [38] and itself can only generate a decrease of the material average of the effective g tensor. Indeed, according to Eq. (1), we obtain $g_{av}^{\mathrm{ND1}} = -0.289$ and $g_{av}^{\mathrm{ND2}} = -0.317$. However, in this estimation, two major factors (and their interplay) are ignored: (a) the wave-function transformation is coupled to the electron confinement energy change (see Fig. 3), which leads to a change of the $g_B(\mathbf{r},E)$; (b) the spin-orbit coupling in the highly nonhomogeneous nanostructures can considerably modify the overall effective g factor. The factors are natural consequences of the electron-hole band coupling in the $\mathbf{k}\cdot\mathbf{p}$ theory. Both factors are incorporated in our model and into expressions for the expectation value of the g-factor tensor in Eqs. (17)–(23).

TABLE II. Electron characteristic lengths in ND1 and ND2 (all in nanometers).

Length	ND1	ND2
d_z	3.3	3.1
d_ρ	5.7	4.6
d	6.6	5.5

TABLE III. Electron effective g factor and anisotropy ratio in ND1 and ND2.

Parameter	ND1	ND2
$\bar{g}_B$	−0.184	−0.175
g_{zz}	−0.063	0.037
g_{xx}	−0.051	0.038
g_{exp}[a]	−0.05	0.1
P_{zx}	0.105	−0.013

[a]Experimental data for $\mathbf{B} \,||\, \hat{\mathbf{z}}$ from Ref. [38].

In the GaAs/$Al_xGa_{1-x}As$ NDs (according to our calculation experience), the Dresselhaus spin-orbit contribution to the electron effective g factor is insignificant and can be ignored. Therefore, the spin-orbit coupling for the NDs is presented in the g-factor tensor only by $\hat{g}^R(\mathbf{r},E_0)$. In addition, owing to the NDs' cylindrical symmetry: $g_{xx} = g_{yy}$ ($P_{zx} = P_{zy}$, $P_{xx} = P_{yy} = 0$) and all expectation values of the off-diagonal components of the g-factor tensor are obviously zero.

Now we show in Table III the expectation values of the material term in the electron effective g factor, $\bar{g}_B = \langle g_B(\mathbf{r},E_0) + \delta g_B(\mathbf{r})\rangle$, diagonal components of the electron effective g-factor tensor, and the tensor anisotropy ratio P_{ij}, when both factors (a) and (b) stated above are taken into consideration. First of all, we have to emphasize a noticeable change in $\bar{g}_B$ from the ND1 to ND2, which is a clear demonstration of the factor (a) impotency. We note that our simulation results of the g_{zz} are in a good agreement with experimental data [38], which confirms a strong impact of the Rashba spin-orbit coupling [the factor (b)]. In addition, we see that within our model, the spin-orbit interaction is responsible for an anisotropy of the electron effective g factor. This is illustrated in Table III. Furthermore, our theoretical model predicts the g_{xx} (g_{yy}) component with a larger value than that of g_{zz}. We also note that the anisotropy ratio in the ND1 and ND2 has a different sign.

The effective g factor for the cylindrical NDs as a function of the magnetic field orientation can be conventionally expressed by its components along the tensor principal axes as the following [66]:

$$g = \sqrt{(g_{xx}B_x)^2 + (g_{yy}B_y)^2 + (g_{zz}B_z)^2}/|\mathbf{B}|. \qquad (24)$$

The g-factor tensors of the electron ground state for the NDs are shown by contour plots in Fig. 4. More details on the anisotropy can be assessed by cuts through the contours along particular planes, also presented in Fig. 4. Notably, the g factor of the ND2 (ND with the noticeable anisotropic electron wave-function distribution; see Fig. 3) is nearly isotropic, while the ND1 g factor still shows some anisotropy.

These findings can be clarified from the expression for the expectation value of the Rashba part to the effective g-factor tensor. According to Eqs. (18) and (20), the averaged $\Lambda_{ii}(\mathbf{r},E_0)$ reads

$$\langle \Lambda_{ii}(\mathbf{r},E)\rangle = \frac{1}{2}\int_V d^3\mathbf{r}\left|\Psi_{E_0}(\mathbf{r})\right|^2 \nabla_i g_B(\mathbf{r},E_0)\cdot R_i. \qquad (25)$$

For the hard-wall confinement, all material parameters of the NDs possess a steplike change at the boundaries of

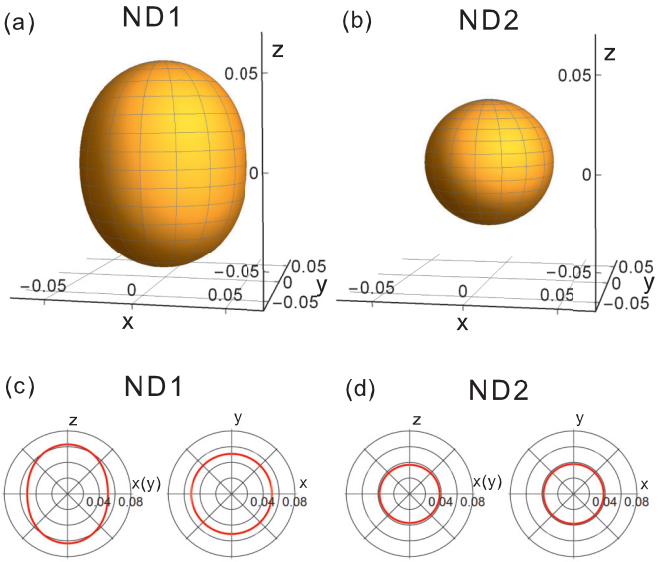

FIG. 4. (Color online) The ground-state electron g-factor tensor as a function of the magnetic field direction: (a),(b) three-dimensional polar plots for ND1 and ND2; (c),(d) cross sections of the three-dimensional plots by the z-$x(y)$ and y-x planes.

the NDs. Therefore, we can suggest that $\nabla_i g_B(\mathbf{r}, E_0) = [g_B(\mathbf{r}^+_{S_i}, E_0) - g_B(\mathbf{r}^-_{S_i}, E_0)]\delta(\xi_i - \xi_{S_i})$, where $\xi_i = \{x, y, z\}$, and the index S_i refers to the appropriate surface of the ND's boundary. Actually, for the steplike changes of the parameters, the derivative is not zero only at the boundary surfaces. Therefore, the averaged $\Lambda_{ii}(\mathbf{r}, E_0)$ also can be presented as an average over the boundary surfaces when the g_B has steplike jumps along the ξ_i direction:

$$\langle \Lambda_{ii}(\mathbf{r}, E_0) \rangle = \frac{1}{2} \int_{S_i} d^2\mathbf{r} \left|\Psi_{E_0}\right|^2 \left[g_B\left(\mathbf{r}^+_{S_i}, E_0\right) - g_B\left(\mathbf{r}^-_{S_i}, E_0\right) \right] \cdot (\mathbf{r} - \bar{\mathbf{r}})_i . \quad (26)$$

It follows from Eq. (26) that the actual impact of the Rashba spin-orbit coupling on the g factor is a result of the interplay between the near-surface change of the $g_B(\mathbf{r})$ and the actual distribution of the electron ground-state probability density in the moment integral (26).

For the ND1, the neighborhood is isotropic. However, the xx and zz moment integrals are different because the ND has obviously different effective sizes in the lateral and vertical directions (see Table II). This causes an anisotropy in the effective g factor for the ND1. Now we can see that for the ND2 (unlike for the ND1), the change in the material parameters at the boundaries in the z direction is considerably smaller then that in the lateral direction (see Fig. 1 and Table I). At the same time, the electron wave-function extension is distinctly less in the lateral direction than that in the z direction (see Table II). These two values interplay in the moment integral, which finally forms an almost isotropic g factor in the ND2.

Based on our model and findings above, we are now able to give useful insight into a possible range of engineering of the electron effective g factor in the high-quality GaAs/$Al_xGa_{1-x}As$ NDs. In a line with the ND1 and ND2, we further propose and explore ND3–ND6 structures (see Fig. 5). In this set, two structures (ND3 and ND6) are reflection nonsymmetrical (with respect to reflections in the x-z and y-z planes). This asymmetry in the confinement potential obviously deforms the electron ground-state probability density distribution along the z direction (see Fig. 5), which shifts the expectation value of the position of the electron in the ground state from the center of the NDs: $\bar{\mathbf{r}} = (0, 0, \bar{z} \neq 0)$. In the following, we will show that our model can also give clear hints of the possible impact of the structural asymmetry on the g-factor anisotropy.

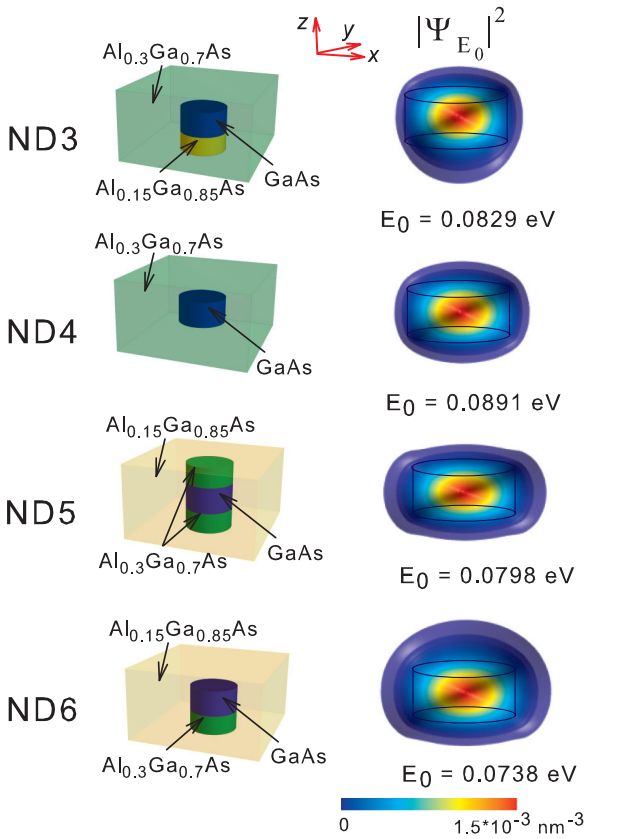

FIG. 5. (Color online) Schematic of the structures ND3–ND6 (left panels) and corresponding probability density distribution for the electron ground state (right panels). The electron ground-state energies are presented correspondingly.

Table IV presents all relevant characteristics for this study of the aforementioned set ND3–ND6. The variations of the electron energy in the ground state within the set are confirmed

TABLE IV. Characteristics of ND3–ND6.

Parameter	ND3	ND4	ND5	ND6
$\bar{z}$ (nm)	−0.7	0.0	0.0	+0.8
d_z (nm)	2.8	2.4	2.6	3.1
d_ρ (nm)	4.6	4.6	6.0	5.8
d (nm)	5.4	5.2	6.5	6.6
$\bar{g}_B$	−0.164	−0.152	−0.157	−0.171
g_{zz}	0.055	0.081	0.023	−0.004
g_{xx}	0.075	0.127	0.135	0.105
P_{zx}	−0.153	−0.221	−0.709	−1.079

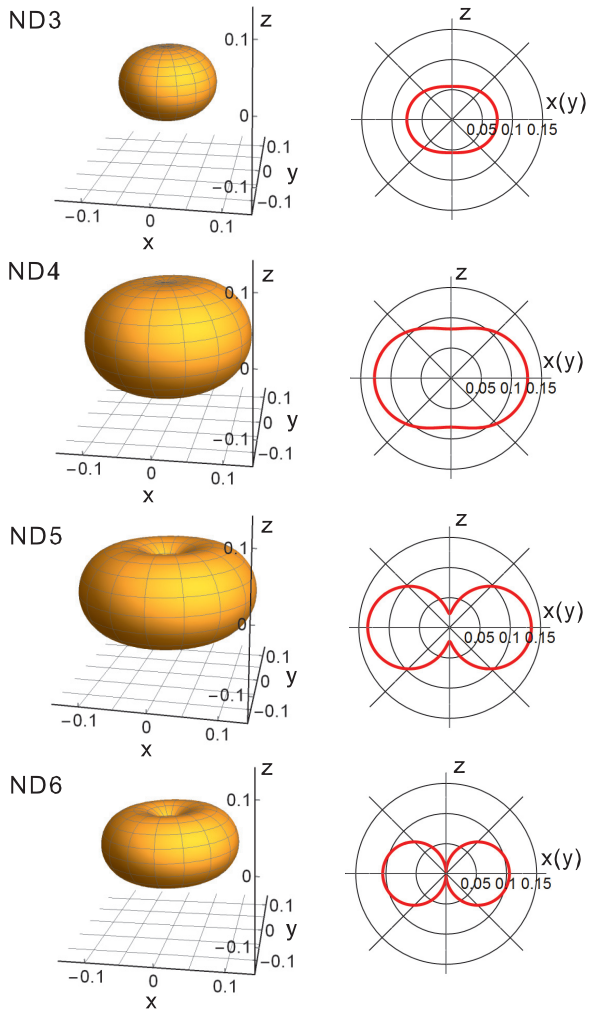

FIG. 6. (Color online) g-factor tensor as a function of the magnetic field direction for the set of ND3–ND6: three-dimensional polar plots (left panels) and cross sections by the z-$x(y)$ and y-plane (right panels; we omit the y-x plane cross sections since the g factor possesses the axial symmetry).

by the variation of the characteristic lengths in the NDs. The reflection asymmetry in the structure with the ND3 generates a reduction of d_z (and, consequently, of d) in respect to that in the ND2 (and, in addition, the relocation of the electron mean position). This is followed by an increase of the electron energy (Fig. 5) and $\bar{g}_B$ (Table IV). Finally, including the Rashba spin-orbit interaction, we arrive at a larger (than that in the ND2) $g_{xx(zz)}$. Following the general properties of the moment integrals in Eq. (26), the asymmetry ratio in the ND3 is larger than that in the ND1 and ND2.

Within the set, the largest electron confinement energy is in the ND4. Therefore, it is not surprising that this ND has the largest g_B in the set (and in this study as well). The interplay of the extension of the electron wave function and material parameters in the structure leads to the largest in the set g_{zz} and a considerable asymmetry ratio (as it was discussed above).

The ND5 properties follow the main tendency in the set. The anisotropy in the material surroundings (which is clear from Fig. 5) leads to an anisotropic transformation in the electron probability distribution (a large difference between d_z and d_ρ) and increase of the asymmetry ratio P_{zx}.

The relatively large asymmetry of the ND6 in the z direction has a clear impact on the ND's characteristics. This ND structure has a very large anisotropy ratio. In addition, we have to note that among all NDs considered in this study, only in the ND6, the g_{zz} and g_{xx} components of the electron effective g-factor tensor have different signs.

Figure 6 clearly illustrates the above-described transformations in the effective g-factor tensor of the electron ground state for the set of NDs. This transformation is presented by contour plots and by cuts of the plots along particular planes. We can observe a strong sensitivity of the tensor to the structural changes in the system. Furthermore, from the results presented in Table II, Table IV, Fig. 4, and Fig. 6, it is clear that the electron effective g-factor tensor components' magnitudes and signs can be tuned by a proper environment design.

IV. CONCLUSION

In this paper, using the effective 2×2 conduction-band Hamiltonian which includes the Rashba and Dresselhaus spin-orbit couplings, we simulated the electron ground-state effective g factor for defect-free GaAs nanodisks with different surroundings. We have systematically investigated the impact of the nanodisks' environmental changes on the electron ground-state wave-function extension, energy, and effective g-factor tensor components. Two types of nanodisks known from experimental works were considered first: with isotropic environment and with non-isotropic environment. Using our theoretical model, we are able to explain how changes in the nanodisk environment lead to the noticeable transformation of the effective g-factor tensor. The transformation is mainly controlled by the electron confinement energy change and Rashba spin-orbit interaction. The Rashba spin-orbit interaction is also responsible for the anisotropy of the electron g factor. The actual values of the effective g-factor tensor components and anisotropy ratio are shown to be results of the interplay between the material parameters' changes near the nanodisks' boundary surface and the actual extension of the electron ground-state wave function. Our model reveals this interplay in a very clear and natural manner. Therefore, the model can characterize general physical tendencies which are useful for further engineering and advanced simulation of the electron effective g factor. We note that our simulation results for the nanodisks in the isotropic and anisotropic structures are in a good agreement with experimental observations.

In addition, in this paper, we proposed a set of defect-free nanodisk structures that can be investigated using the same experimental technique. We demonstrated that the control of symmetry and anisotropy of the nanodisks' environment in the defect-free structures can give us a unique opportunity for advancement in the tuning of the electron effective g factor of the nanodisks. Extra flexibility can be achieved by variation of the actual sizes of the nanodisks themselves. This makes the defect-free GaAs nanodisk structures very interesting and promising objects for investigation of the controllability of the

electron small g factor in massive arrays of the semiconductor nano-objects.

We emphasize that using our model, we are able to clarify the important question of the material and geometrical parameter interplay in the formation of the electron effective g factor in semiconductor nano-objects. More generally, our model can be applied to the realistic and efficient modeling of the magnetic response of semiconductor nano-objects with nonsymmetric and anisotropic geometry and material content.

ACKNOWLEDGMENTS

This work is supported in part by the WPI-Advanced Institute for Materials Research of the Tohoku University. It is also supported by the Ministry of Science and Technology, Taiwan, under Contracts No. NSC 102-2112-M-009-004-MY2 and No. MOST 103-2221-E-009-180, and by Aiming for the Top University Program of the National Chiao Tung University.

[1] *Quantum Dots Optics, Electron Transport and Future Applications*, edited by A. Tartakovskii (Cambridge University Press, Cambridge, 2012).
[2] *Physics of Quantum Rings*, edited by Vladimir M. Fomin (Springer, Berlin, 2014).
[3] *Quantum Dot Molecules*, edited by Jiang Wu and Zhiming M. Wang (Springer, Berlin, 2014).
[4] *Semiconductor Nanowires: From Next-Generation Electronics to Sustainable Energy, RSC Smart Materials*, edited by Wei Lu and Jie Xiang (Royal Society of Chemistry, London, 2014).
[5] *Manipulating Quantum Coherence in Solid State Systems*, edited by M. E. Flatté and I.Ţifrea (Springer, Berlin, 2005).
[6] R. Hanson, L. P. Kouwenhoven, J. R. Petta, S. Tarucha, and L. M. K. Vandersypen, Rev. Mod. Phys. **79**, 1217 (2007).
[7] R. J. Warburton, Nat. Mater. **12**, 483 (2013).
[8] D. Loss and D. P. DiVincenzo, Phys. Rev. A **57**, 120 (1998).
[9] S. Nadj-Perge, S. M. Frolov, E. P. A. M. Bakkers, and L. P. Kouwenhoven, Nature (London) **468**, 1084 (2010).
[10] T. D. Ladd, F. Jelezko, R. Laflamme, Y. Nakamura, C. Monroe, and J. L. O'Brien, Nature (London) **464**, 45 (2010).
[11] C. Kloeffel and D. Loss, Annu. Rev. Condens. Matter Phys. **4**, 51 (2013).
[12] *Semiconductor Spintronics and Quantum Computation*, edited by D. D. Awschalom, N. Samarth, and D. Loss (Springer-Verlag, Heidelberg, 2002).
[13] J. Fabian, A. Matos-Abiaguea, C. Ertlera, P. Stano, and I. Žutić, Acta Phys. Slov. **57**, 565 (2007).
[14] D. D. Awschalom and M. E. Flatté, Nat. Phys. **3**, 153 (2007).
[15] J. Xia, W. Ge, and K. Chang, *Semiconductor Spintronics* (World Scientific, New Jersey, 2012).
[16] D. Awschalom, L. C. Bassett, A. S. Dzurak, E. L. Hu, and J. R. Petta, Science **339**, 1174 (2013).
[17] G. Dresselhaus, Phys. Rev. **100**, 580 (1955).
[18] Y. A. Bychkov and E. I. Rashba, J. Phys. C **17**, 6039 (1984).
[19] R. Winkler, *Spin-Orbit Coupling Effects in Two-Dimensional Electron and Hole Systems* (Springer, Berlin, 2003).
[20] Y. Kanai, R. S. Deacon, S. Takahashi, A. Oiwa, K. Yoshida, K. Shibata, K. Hirakawa, Y. Tokura, and S. Tarucha, Nat. Nanotechnol. **6**, 511 (2011).
[21] R. S. Deacon, Y. Kanai, S. Takahashi, A. Oiwa, K. Yoshida, K. Shibata, K. Hirakawa, Y. Tokura, and S. Tarucha, Phys. Rev. B **84**, 041302(R) (2011).
[22] A. A. Kiselev, E. L. Ivchenko, and U. Rössler, Phys. Rev. B **58**, 16353 (1998).
[23] C. E. Pryor and M. E. Flatté, Phys. Rev. Lett. **96**, 026804 (2006).
[24] T. P. Mayer Alegre, F. G. G. Hernández, A. L. C. Pereira, and G. Medeiros-Ribeiro, Phys. Rev. Lett. **97**, 236402 (2006).
[25] I. A. Yugova, A. Greilich, D. R. Yakovlev, A. A. Kiselev, M. Bayer, V. V. Petrov, Yu. K. Dolgikh, D. Reuter, and A. D. Wieck, Phys. Rev. B **75**, 245302 (2007).
[26] *Electron Spin Resonance and Related Phenomena in Low-Dimensional Structures*, edited by M. Fanciulli (Springer, Berlin, 2009).
[27] W. Sheng, Appl. Phys. Lett. **94**, 123113 (2009).
[28] S. Takahashi, R. S. Deacon, K. Yoshida, A. Oiwa, K. Shibata, K. Hirakawa, Y. Tokura, and S. Tarucha, Phys. Rev. Lett. **104**, 246801 (2010).
[29] A. Schwan, B.-M. Meiners, A. Greilich, D. R. Yakovlev, M. Bayer, A. D. B. Maia, A. A. Quivy, and A. B. Henriques, Appl. Phys. Lett. **99**, 221914 (2011).
[30] J. Pingenot, C. E. Pryor, and M. E. Flatté, Phys. Rev. B **84**, 195403 (2011).
[31] S. Takahashi, R. S. Deacon, A. Oiwa, K. Shibata, K. Hirakawa, and S. Tarucha, Phys. Rev. B **87**, 161302(R) (2013).
[32] R. Zielke, F. Maier, and D. Loss, Phys. Rev. B **89**, 115438 (2014).
[33] G. Allison, T. Fujita, K. Morimoto, S. Teraoka, M. Larsson, H. Kiyama, A. Oiwa, S. Haffouz, D. G. Austing, A. Ludwig, A. D. Wieck, and S. Tarucha, Phys. Rev. B **90**, 235310 (2014).
[34] J. H. Prechtel, F. Maier, J. Houel, A. V. Kuhlmann, A. Ludwig, A. D. Wieck, D. Loss, and R. J. Warburton, Phys. Rev. B **91**, 165304 (2015).
[35] S. Samukawa, ECS J. Solid State Sci. Technol. **4**, N5089 (2015).
[36] T. Kaizu, Y. Tamura, M. Igarashi, W. Hu, R. Tsukamoto, I. Yamashita, S. Samukawa, and Y. Okada, Appl. Phys. Lett. **101**, 113108 (2012).
[37] Y. Tamura, T. Kaizu, T. Kiba, M. Igarashi, R. Tsukamoto, A. Higo, W. Hu, C. Thomas, M. E. Fauzi, T. Hoshii, I. Yamashita, Y. Okada, A. Murayama, and S. Samukawa, Nanotechnology **24**, 285301 (2013).
[38] T. Tanaka, T. Kiba, A. Higo, C. Thomas, Y. Tamura, S. Samukawa, and A. Murayama, J. Crystallogr. Growth **425**, 295 (2015).
[39] E. L. Ivchenko, *Optical Spectroscopy of Semiconductor Nanostructures* (Alpha Science International, Harrow, UK, 2005).
[40] A. A. Kiselev, K. W. Kim, and E. Yablonovitch, Appl. Phys. Lett. **80**, 2857 (2002).
[41] L. M. Roth, B. Lax, and S. Zwerdling, Phys. Rev. **114**, 90 (1959).
[42] Lok C. Lew Yan Voon and Morten Willatzen, *The kp Method. Electronic Properties of Semiconductors* (Springer, Heidelberg, 2009).
[43] C. Hermann and C. Weisbuch, Phys. Rev. B **15**, 823 (1977).
[44] H. Kosaka, A. A. Kiselev, F. A. Baron, K. W. Kim, and E. Yablonovitch, Electron. Lett. **37**, 464 (2001).

[45] V. Mlinar, M. Tadić, B. Partoens, and F. M. Peeters, Phys. Rev. B **71**, 205305 (2005).
[46] R. G. Veprek, S. Steiger, and B. Witzigmann, Phys. Rev. B **76**, 165320 (2007).
[47] *Multi-Band Effective Mass Approximations. Advanced Mathematical Models and Numerical Techniques*, edited by M. Ehrhardt and T. Koprucki (Springer, Heidelberg, 2014).
[48] M. de Dios-Leyva, E. Reyes-Gómez, C. A. Perdomo-Leiva, and L. E. Oliveira, Phys. Rev. B **73**, 085316 (2006).
[49] P. Pfeffer and W. Zawadzki, Phys. Rev. B **74**, 233303 (2006).
[50] J. R. Mejá-Salazar, N. Porras-Montenegro, and L. E. Oliveira, J. Phys.: Condens. Matter **21**, 455302 (2009).
[51] G. Bastard, *Wave Mechanics Applied to Semiconductor Heterostructures* (Les Edition de Physique, Les Ulis, 1990).
[52] E. A. de Andrada e Silva, G. C. La Rocca, and F. Bassani, Phys. Rev. B **50**, 8523 (1994).
[53] Th. Schäpers, G. Engels, J. Lange, Th. Klocke, M. Hollfelder, and H. Lüth, J. Appl. Phys. **83**, 4324 (1998).
[54] Y. Li. Voskoboynikov, C. P. Lee, S. M. Sze, and O. Tretyak, Eur. Phys. J. B **28**, 475 (2002).
[55] O. Voskoboynikov, Y. Li, H. M. Lu, C. F. Shih, and C. P. Lee, Phys. Rev. B **66**, 155306 (2002).
[56] H. C. Huang, O. Voskoboynikov, and C. P. Lee, Phys. Rev. B **67**, 195337 (2003).
[57] J. I. Clemente, J. Planelles, and J. L. Movilla, Phys. Rev. B **70**, 081301 (2004).
[58] O. Voskoboynikov, W. T. Chiu, and L. M. Thu, Phys. Rev. B **88**, 085310 (2013).
[59] M. A. Toloza Sandoval, A. Ferreira da Silva, E. A. de Andrada e Silva, and G. C. La Rocca, Phys. Rev. B **86**, 195302 (2012).
[60] E. Ridolfi, E. A. de Andrada e Silva, and G. C. La Rocca, Phys. Rev. B **91**, 085313 (2015).
[61] I. Vurgaman, J. R. Meyer, and L. R. Ram-Mohan, J. Appl. Phys. **89**, 5815 (2001).
[62] O. Voskoboynikov, C. P. Lee, and O. Tretyak, Phys. Rev. B **63**, 165306 (2001).
[63] Y. Li, O. Voskoboynikov, C. P. Lee, and S. M. Sze, Comput. Phys. Commun. **141**, 66 (2001).
[64] http://www.comsol.com.
[65] Y. Li, J. L. Liu, O. Voskoboynikov, C. P. Lee, and S. M. Sze, Comput. Phys. Commun. **140**, 399 (2001).
[66] M. D. Schroer, K. D. Petersson, M. Jung, and J. R. Petta, Phys. Rev. Lett. **107**, 176811 (2011).